

Ultralow shear modulus of incommensurate $[\text{SnSe}]_n[\text{MoSe}_2]_n$ layers synthesized by the method of modulated elemental reactants

Dongyao Li, André Schleife, and David G. Cahill*

Department of Materials Science and Engineering and Materials Research Laboratory, University of Illinois, Urbana, Illinois 61822, USA

Gavin Mitchson and David C. Johnson

Materials Science Institute and Department of Chemistry, University of Oregon, Eugene, Oregon 97403, USA



(Received 11 February 2019; published 26 April 2019)

We demonstrate that the shear elastic constant of misfit-layered dichalcogenide films $[\text{SnSe}]_n[\text{MoSe}_2]_n$ with $n = 1, 2, 3$, synthesized by the modulated elemental reactants method, is $c_{44} \approx 1$ GPa, an order of magnitude lower than c_{44} of typical layered crystals that have weak interlayer van der Waals bonding. The films are synthesized by alternating deposition of the elements to a total thickness of ≈ 60 nm followed by thermal annealing. We determine c_{44} through measurements of the velocities of 700 nm wavelength surface acoustic waves propagating along the surface of $\text{Al}/[\text{SnSe}]_n[\text{MoSe}_2]_n/\text{Si}$ structures in combination with picosecond acoustics measurements of c_{33} and calculations of the c_{11} , c_{12} , and c_{13} elastic constants by density functional theory. We attribute the low value of c_{44} to incommensurate interfaces between SnSe and MoSe₂ layers and turbostratic disorder within the MoSe₂ layers. We conclude that the ultralow shear modulus of disordered layered materials contributes significantly to their exceptionally low thermal conductivity.

DOI: [10.1103/PhysRevMaterials.3.043607](https://doi.org/10.1103/PhysRevMaterials.3.043607)

I. INTRODUCTION

Layered materials with turbostratic disorder [1] and incommensurate interfaces [2] have been shown to have exceptionally low thermal conductivity in the direction normal to their interfaces. For example, the through-plane thermal conductivity Λ_{\perp} of disordered layered WSe₂ can be as low as $\Lambda_{\perp} \approx 0.05 \text{ W m}^{-1} \text{ K}^{-1}$, comparable to the lowest Λ ever observed in a fully dense material and only a factor of 2 higher than the thermal conductivity of air. The origin of this ultralow Λ_{\perp} is currently thought to arise from the combination of atomic-scale disorder and the strong anisotropy in the elastic constants between the in-plane and through-plane directions that suppresses the average phonon group velocity in the through-plane direction. This suppression of transport in the elastically soft direction relative to the elastically stiff direction is often referred to as “phonon focusing” [3–9].

Knowledge of the elastic constants of layered materials is needed to evaluate the significance of phonon-focusing effects on Λ_{\perp} . Our original paper [1] on the ultralow thermal conductivity of disordered layered WSe₂ includes an estimate of the minimum thermal conductivity for the through-thickness direction where we assumed that the ratio of the longitudinal to shear elastic constants was independent of microstructure. In other words, we did not consider the effect of turbostratic disorder on the shear modulus. Stacking disorder is likely to have a strong effect: Savini *et al.* [10] calculated the elastic constants of graphite with turbostratic disorder and concluded that c_{44} can be as low as ≈ 0.2 GPa, a factor of ≈ 20 lower than well crystallized graphite [11,12].

The longitudinal speed of sound in the through-thickness direction, $v_l^2 = \rho c_{33}$, of thin films can be conveniently measured using picosecond acoustics [13]. Measurements of the transverse speed of sound $v_t^2 = \rho c_{44}$ along the direction normal to the surface are, however, much more difficult [14]. The velocity of surface acoustic waves (SAWs) provides an alternative approach; the SAW velocity v_{SAW} is typically sensitive to c_{44} [15]. To increase the sensitivity of v_{SAW} to the elastic constants of a thin layer requires that the penetration depth of the stress field of the SAW is comparable to the layer thickness [16]. This penetration depth is on the order of the SAW wavelength divided by π . In the present work, we use SAW with a wavelength of 700 nm and a frequency of ≈ 4 GHz to probe the elastic constants of incommensurate layered materials with a thickness less than 100 nm.

The $[\text{SnSe}]_n[\text{MoSe}_2]_n$ system provides a useful target material for our study [2]. By varying n , we can evaluate systematic trends in the shear elastic constant for incommensurate SnSe/MoSe₂ interfaces and MoSe₂ interfaces with turbostratic disorder.

II. EXPERIMENT

A. Film synthesis and characterization

Compositionally modulated precursors targeting the $[\text{SnSe}]_n[\text{MoSe}_2]_n$ $n = 1, 2, 3$ compounds were prepared using the modulated elemental reactants (MER) technique [17,18]. The specific methods for preparing SnSe and MoSe₂-containing misfit layer compounds (MLCs) using this technique were reported previously [2,17]. In brief, precursor synthesis is conducted using a custom-built high vacuum deposition chamber (base pressure $\approx 10^{-7}$ Torr) containing multiple deposition sources. To build the precursor, a Si

*d-cahill@illinois.edu

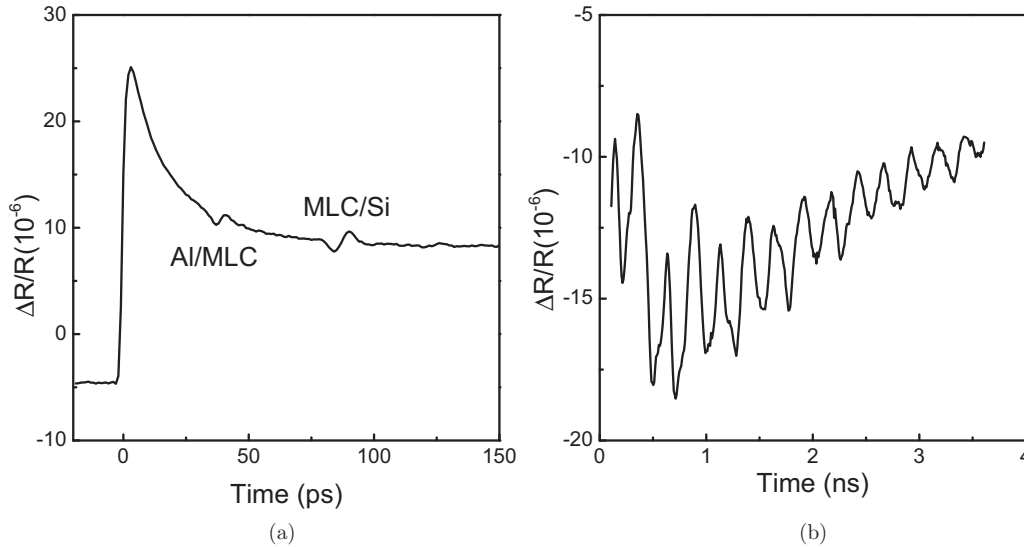


FIG. 1. (a) Typical signal of longitudinal acoustic echo measurement of an Al/MLC/Si sample structure. The label MLC refers to “misfit layer compound.” (b) Typical signal of SAW measurement of the same sample structure.

substrate is mounted to a motorized carousel that drives the substrate to each source. Pneumatically controlled shutters are used to control the amount of material deposited onto the substrate. The substrate is moved from source to source in a sequence designed to build a layered structure. After deposition, the precursors were transferred through air to a nitrogen (<1 ppm O_2) atmosphere and annealed on a calibrated hotplate at 400°C for 20 min.

Film thicknesses and c -axis lattice parameters were determined from specular x-ray reflectivity (XRR) and x-ray diffraction (XRD) scans acquired using a Bruker D8 Discover diffractometer (Cu K_α radiation). We use the positions of the Kiessig fringes to determine the film thickness [19]. The c -axis lattice parameters are determined from the XRD scan peak locations using Bragg’s law. In-plane lattice parameters were determined using grazing incidence in-plane XRD scans acquired using a Rigaku Smartlab diffractometer (Cu K_α radiation) and analyzed using least-squares regression of peak locations in WinCSD [20]. The misfit ratios were calculated from the ratios of the basal plane areas of the SnSe and MoSe₂ constituents: the SnSe basal plane area is slightly smaller than that of the MoSe₂; therefore, to cover the same area, slightly more SnSe is required than MoSe₂ and the misfit parameter δ is a small positive number. Sample compositions were measured using x-ray fluorescence (XRF) on a Rigaku ZSX-II calibrated for thin films containing Sn, Mo, and Se. High-angle annular dark field scanning transmission electron microscopy (HAADF-STEM) was used to study the microstructure of the film.

B. Elastic constants measurement

To relate the surface acoustic wave velocity to the elastic constants, we model the elasticity of the $[\text{SnSe}]_n[\text{MoSe}_2]_n$ layer as an effective medium with textured hexagonal symmetry. A textured polycrystalline hexagonal material with (001) texture has five independent elastic constants: c_{11} , c_{12} , c_{13} , c_{33} , and c_{44} . We measure c_{33} using picosecond acoustics [13] and

c_{44} using a SAW technique [16]. Both of the measurements are done using an ultrafast pump-probe apparatus based on a Ti:sapphire laser oscillator as the light source [21].

Prior to both picosecond acoustics and SAW measurements, a layer of Al, ≈ 140 nm thick, is sputtered on top of the $[\text{SnSe}]_n[\text{MoSe}_2]_n/\text{Si}$ sample to serve as a transducer that converts heat from the pump laser beam to thermoelastic strain. In the picosecond acoustics experiments, the Al layer also converts near-surface stress to a change in optical reflectivity of the probe laser beam [13]. The pump and probe beams are focused onto the sample surface with $1/e^2$ intensity radius of $w_0 \approx 11 \mu\text{m}$. The longitudinal acoustic pulse that is generated by the pump optical pulse travels through the Al/ $[\text{SnSe}]_n[\text{MoSe}_2]_n/\text{Si}$ sample structure and reflects from the Al/ $[\text{SnSe}]_n[\text{MoSe}_2]_n$ and $[\text{SnSe}]_n[\text{MoSe}_2]_n/\text{Si}$ interfaces. The return of the reflected acoustic pulse, i.e., the acoustic echo, to the sample surface is measured by the probe optical pulse. Figure 1(a) shows representative picosecond acoustics data. We determine the round-trip acoustic travel time t_l in the $[\text{SnSe}]_n[\text{MoSe}_2]_n$ film by taking the difference in the arrival time of the two echoes. The velocity of the longitudinal acoustic wave is $v_l = 2h/t_l$, where h is the film thickness, and the corresponding elastic constant is $c_{33} = \rho v_l^2$, where ρ is the density of the $[\text{SnSe}]_n[\text{MoSe}_2]_n$ calculated from the measured composition and lattice constants.

We use an elastomeric optical phase shift mask to generate and detect SAW [16]. The polydimethylsiloxane (PDMS) mask is fabricated using a commercially available Si master (Lightsmlyth) as a mold. The Si master is a nanofabricated grating with a period of 700 nm, duty cycle of 50%, and depth of 350 nm. For a $[\text{SnSe}]_n[\text{MoSe}_2]_n$ layer with a thickness of ≈ 60 nm, the optimal thickness of the Al layer is relatively thick, ≈ 145 nm, to enhance the sensitivity of SAW velocity to the shear elastic constants of the layer under study [22]. The mask is adhered to the sample surface and the time domain signal generated by the propagation of SAW with wavelength $\lambda = 0.7 \mu\text{m}$ is measured in the pump-probe system. The velocity of SAW is $v_{\text{SAW}} = \lambda f$ where f is the SAW frequency.

A typical signal acquired in the SAW measurement is shown in Fig. 1(b). Further details of our method for measuring SAW velocities can be found in Ref. [16].

Typically, v_{SAW} is sensitive to shear elastic constants [15]. We calculate v_{SAW} of an arbitrary layered structure using a Green's function method [23,24] and extract the shear elastic constants by fitting the calculated v_{SAW} to the measured v_{SAW} . The model has 16 parameters: 3 elastic constants each for the Al layer and Si substrate; 5 elastic constants of $[\text{SnSe}]_n[\text{MoSe}_2]_n$; the densities of the three materials; and the thicknesses of the Al and $[\text{SnSe}]_n[\text{MoSe}_2]_n$ layers. We define the sensitivity S of v_{SAW} to an elastic constant c_{ij} as

$$S(c_{ij}) = \frac{\partial \ln(v_{\text{SAW}})}{\partial \ln(c_{ij})}. \quad (1)$$

In the sample structure with a 145 nm thick Al layer, and setting $c_{44} = 1$ GPa, the sensitivities of v_{SAW} to the elastic constants of the 60 nm thick $[\text{SnSe}]_n[\text{MoSe}_2]_n$ layer are $S(c_{33}) = 0.11$, $S(c_{44}) = 0.03$, and $S(c_{11}) \approx 0.03$; the sensitivities to c_{12} and c_{13} are $S < 10^{-3}$. We use picosecond acoustics to measure c_{33} with high accuracy. While c_{44} has the highest sensitivity parameter other than c_{33} , we still need estimates of c_{11} , c_{12} , and c_{13} , with c_{11} being by far the most important, to determine c_{44} from the measured v_{SAW} . In Sec. III we describe our use of density functional theory to calculate c_{11} , c_{12} , and c_{13} .

III. CALCULATION OF ELASTIC CONSTANTS BY DENSITY FUNCTIONAL THEORY

We calculate the elastic constants of $[\text{SnSe}]_1[\text{MoSe}_2]_1$ and MoSe_2 using density functional theory (DFT) and the harmonic approximation

$$E(V, \epsilon) = E(V_0) + V_0 \sum_{i=1}^6 \sigma_i \epsilon_i + \frac{V_0}{2} \sum_{i,j=1}^6 c_{ij} \epsilon_i \epsilon_j, \quad (2)$$

where E is the total energy of the system, V_0 is the equilibrium unit-cell volume, σ is the stress tensor, ϵ is the strain tensor, and c_{ij} is the reduced form of the rank-four elastic constants tensor. The elastic constants are calculated from the second derivatives of the internal energy with respect to strain, where ϵ_i is written as a vector with six elements.

Our DFT calculations for the 20 atom unit cells utilize the projector-augmented wave method (PAW) to describe the electron-ion interaction and the generalized-gradient approximation (GGA) by Perdew, Burke, and Ernzerhof (PBE) [25] to describe exchange and correlation. Kohn-Sham states are expanded into a plane-wave basis with a cutoff of 400 eV and the Brillouin zone is sampled using $4 \times 4 \times 4$ Γ -centered \mathbf{k} -point grids. This leads to total energies that are converged to within 0.3 meV per atom. We use the method of Tkatchenko and Scheffler [26] to model van der Waals forces between atomic layers.

The goal of this aspect of our work is to obtain good estimates of the elastic constants c_{11} , c_{12} , and c_{13} of $[\text{SnSe}]_n[\text{MoSe}_2]_n$ so that we can use experimental values of surface acoustic wave velocities to determine the shear modulus c_{44} . Uncertainties in the van der Waals force between layers do not have a significant effect on the calculation of

c_{11} , which is the most important unknown in the analysis of SAW data. Therefore, even if the van der Waals forces are not captured accurately, we expect that the calculated values of c_{11} , c_{12} , and c_{13} will be sufficiently accurate for the model in this work. All DFT simulations are carried out using the Vienna *ab initio* simulation package (VASP) [27,28].

Since $[\text{SnSe}]_n[\text{MoSe}_2]_n$ is incommensurate with a misfit parameter of $\delta \approx 0.05$, it is impractical to perform a DFT calculation for the incommensurate superlattice. For $n > 1$, the calculation is also computationally expensive, and we limit ourselves to the $n = 1$ case. The starting unit cell has trigonal symmetry and consists of one layer of four MoSe_2 formula units and one layer of four SnSe formula units with the Sn-Se atoms initially positioned to approximate a layer of a

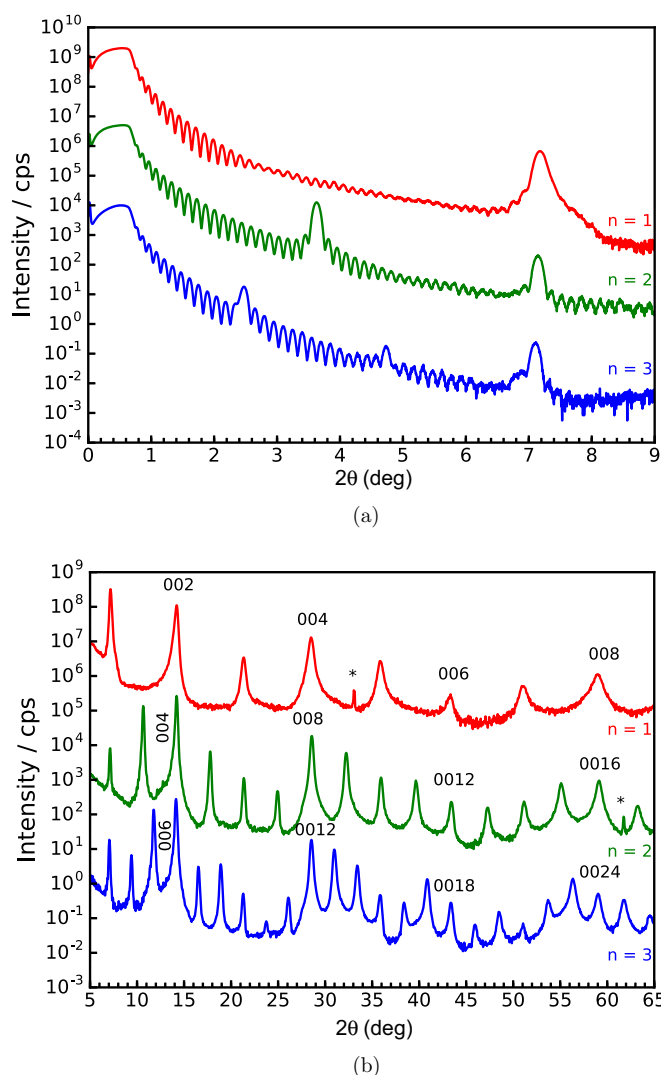


FIG. 2. (a) XRR and (b) XRD scans for $[\text{SnSe}]_n[\text{MoSe}_2]_n$ samples with $n = 1, 2, 3$. Data for $n = 2$ are shifted up by a factor of 1000 relative to $n = 3$, and data for $n = 1$ are shifted up by a factor of 10^6 relative to $n = 3$ to more clearly display the data on a single plot. (a) High-frequency modulation in the intensities as a function of angle are the Kiessig fringes. The higher intensity maxima are Bragg reflections. (b) Selected Bragg reflections are labeled for each scan. The peak labeled by an asterisk is due to the Si substrate.

rock-salt crystal structure. We then relax the atomic positions to minimize Hellman-Feynman forces. The relaxation of the computational cell breaks the three-fold rotational symmetry, resulting in a orthorhombic unit cell with lattice parameters $a = 0.584$, $b = 0.648$, and $c = 1.246$ nm. The areal density of MoSe_2 formula units in the relaxed computational cell is $1.06 \times 10^{15} \text{ cm}^{-2}$, within 1% of the experimental value. Since the computational model is commensurate, the areal density of SnSe formula units is also $1.06 \times 10^{15} \text{ cm}^{-2}$, with $\approx 5\%$ smaller areal density than the experimental value.

To calculate elastic constants, we follow the procedure of Steine-Neumann *et al.* [29]. We first compute total energies for different unit-cell volumes around $\pm 4\%$ of the equilibrium value and fit the Birch-Murnaghan equation of state [30] to these data. This provides us with the bulk modulus of the material. We then calculate elastic constants by straining the equilibrium lattice, relaxing the internal degrees of freedom, and evaluating the change in energy as a function of strain. The strain tensors we used for each set of elastic constants can be found in Ref. [29].

Following the same procedure, we calculated the elastic constants of single crystal MoS_2 to test our methods.

IV. RESULTS AND DISCUSSION

Figure 2 shows the XRR and XRD patterns from the three annealed samples used in this study. Film thicknesses derived from the periodicity of the Kiessig fringes shown in Fig. 2(a) are summarized in Table I. Figure 2(b) shows the high-angle XRD patterns for the three samples. Only Bragg reflections corresponding to $00l$ reflections are present, indicating that the compounds adopt a layered structure with crystallographic alignment to the Si substrate. Indexing the $00l$ Bragg reflections allows determination of the c -axis lattice parameters, see Table I.

The in-plane structure of the compounds are determined from the in-plane XRD patterns shown in Fig. 3. Only reflections corresponding to $hk0$ planes of each constituent are present, providing further evidence of a layered structure with crystallographic alignment to the substrate. Also, the presence of distinct reflections for each constituent indicates that the two constituents are not epitaxially related. The in-plane lattice parameters for the SnSe and MoSe_2 constituents are given in Table I. We indexed the SnSe constituent using a square basal plane and indexed the MoSe_2 constituent using a trigonal basal plane. The SnSe a -axis lattice parameter is similar to that reported for the high-temperature cubic phase

TABLE I. Summary of film thickness, a -axis lattice parameters for each constituent, c -axis lattice parameters, and misfit ratios calculated from the in-plane lattice parameters for $[\text{SnSe}]_n[\text{MoSe}_2]_n$ with $n = 1, 2, 3$.

n	Film thickness (nm)	$\text{SnSe } a$ (nm)	$\text{MoSe}_2 a$ (nm)	c (nm)	Misfit ratio
1	59.8(10)	0.6014(1)	0.331(1)	1.251(1)	1.06(1)
2	58.9(7)	0.6057(3)	0.3334(3)	2.497(2)	1.06(1)
3	57.6(7)	0.605(1)	0.3329(2)	3.752(3)	1.05(1)

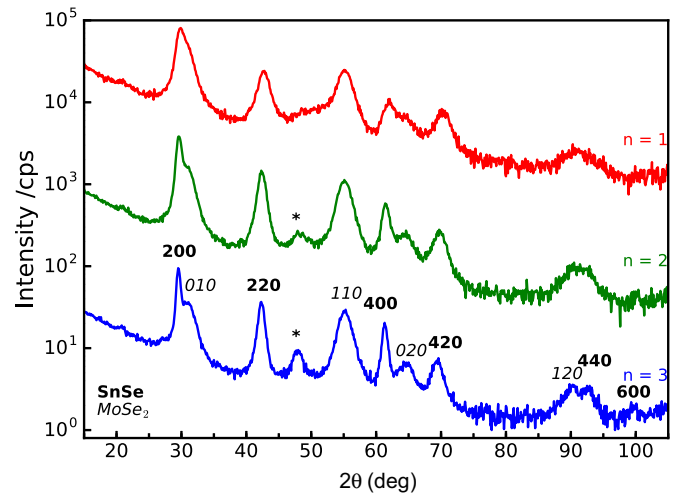


FIG. 3. In-plane XRD scans for the $[\text{SnSe}]_n[\text{MoSe}_2]_n$ samples with $n = 1, 2, 3$. Data for $n = 2$ are shifted up by a factor of 30 relative to $n = 3$, and data for $n = 1$ are shifted up by a factor of 1000 relative to $n = 3$ to more clearly display the data on a single plot. Reflections corresponding to the SnSe constituent are labeled in bold fonts. Reflections corresponding to the MoSe_2 constituent are labeled in italics. The asterisks denote reflections that are classically forbidden in the three-dimensional (3D) SnSe space group, but are allowed if the 3D group is collapsed into a 2D space group [35].

of bulk SnSe , 0.4293(8) nm [31], and agrees with the $\text{SnSe } a$ parameter previously reported for the $[\text{SnSe}]_n[\text{MoSe}_2]_n$ compounds [32]. The MoSe_2 a -axis lattice parameter is similar to the 0.3290(2) nm lattice constant reported for bulk MoSe_2 [33] and the value of 0.332(3) nm previously reported for the $[\text{SnSe}]_n[\text{MoSe}_2]_n$ compounds [32]. Taking the ratio of the basal plane areas yields misfit parameters of $\delta \approx 0.05$, within

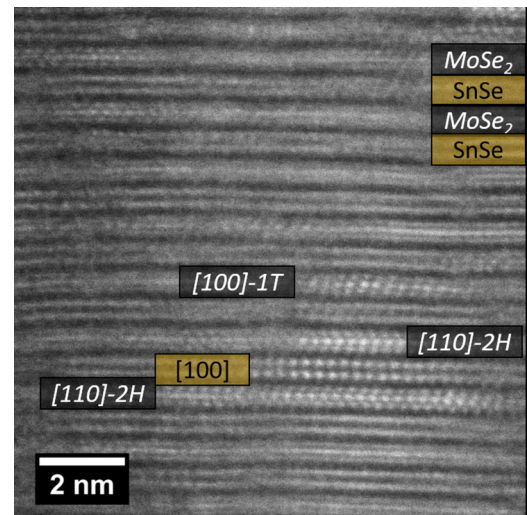


FIG. 4. HAADF-STEM image of $[\text{SnSe}]_n[\text{MoSe}_2]_n$ with $n = 1$. A SnSe layer with a $[100]$ zone axis is labeled by the text “[100]” written in black font on a yellow background. Two regions of MoSe_2 layers with the 2H structure and one region of a MoSe_2 layer with the 1T structure are labeled by the text “[110]-2H” and “[100]-1T”, respectively, written in white fonts on black backgrounds. The labels are placed on top of the layers that they refer to.

TABLE II. Measured and calculated lattice and elastic constants of MoS₂ and comparison with prior work.

	a (Å)	c (Å)	c_{11} (GPa)	c_{12} (GPa)	c_{13} (GPa)	c_{33} (GPa)	c_{44} (GPa)
DFT calculation	3.16	12.05	223	49.9	6.52	52	16.9
Experiment						54	15.4
Volkova calculation [40]	3.18	12.35	214	58		56	18
Feldman experiment [41]			238	-54	23	52	18.6

the range of previously reported values [18,32,34]. The atomic ratios determined using x-ray fluorescence are ≈ 1.1 .

The measured in-plane and through-plane lattice constants of [SnSe]_{*n*}[MoSe₂]_{*n*} are compiled in Table I. The XRD scan suggests the precursor crystallized into a layered film with strong crystallographic alignment to the substrate. Both the c axis and the in-plane lattice parameters of repeating units of each sample are consistent with previously reported values [32]. The XRR scans indicate the samples are high quality with low interface roughness. Based on the derivation of Wainfan and Parratt [36], the film roughness is less than 0.6 nm. The incommensurate in-plane lattice parameters suggest that there is no epitaxial relationship between layers. The ratio of the in-plane areas for the two constituents provides the misfit ratio. We also obtain crystallite sizes from the peak width of the in-plane XRD scan. Neglecting strain effects, which are usually negligible in MER-prepared compounds [32,35], Scherrer analysis indicates that the SnSe grain size increases from 4.5 nm for $n = 1$ to 5.8 nm for $n = 2$ and 6.1 nm for $n = 3$; the MoSe₂ grain size increases from 3.3 nm for $n = 1$ to 3.7 nm for $n = 2$ and 3.9 nm for $n = 3$.

We apply high-angle annular dark field (HAADF) scanning transmission electron microscopy (STEM) to verify structural information. A HAADF-STEM image of a representative $n = 1$ sample is shown in Fig. 4. These imaging data support our conclusion based on x-ray diffraction that the samples are crystallographically aligned to the substrate and consist of alternating layers of rock-salt-like SnSe interleaved with trigonal MoSe₂. The total film thickness is confirmed to be the same as determined from analysis of XRR. There is no apparent relationship between the alignment of grains within one layer and the alignment of grains within an adjacent layer; i.e., the layers are turbostratically disordered. Turbostratic disordering of adjacent dichalcogenide layers prepared by MER was observed previously and is correlated with the ability of the dichalcogenide to form multiple stacking arrangements [37,38].

As a test of our approach of measurements and DFT calculations of elastic constants, we measured the c_{33} and c_{44} elastic constants of an exfoliated MoS₂ crystal and compare our experimental results with our DFT calculations and prior work in Table II. For the measurements, an ≈ 170 nm thick

MoS₂ flake is exfoliated from a bulk MoS₂ crystal on a thermally oxidized Si wafer. The a-SiO₂ thickness is 300 nm. We measure the thickness of the exfoliated flake of MoS₂ by atomic force microscopy (see Supplemental Material [39]). We coated the MoS₂ flake with an Al layer ≈ 135 nm thick. We find good agreement between our experiments and calculations and the prior results [40,41].

We calculated the elastic constants of [SnSe]₁[MoSe₂]₁ by DFT as described in Sec. III and summarize the results in Table III. In the analysis of the v_{SAW} measurements, we make the assumption that c_{11} , c_{12} , and c_{13} of [SnSe]_{*n*}[MoSe₂]_{*n*} do not change significantly with n . To extract c_{44} of [SnSe]_{*n*}[MoSe₂]_{*n*} from the v_{SAW} data, we use measured c_{33} with corresponding n and use the DFT-calculated values of c_{11} , c_{12} , and c_{13} for $n = 1$. The measured c_{33} and the value of c_{44} determined following the procedure described above are plotted in Fig. 5.

The value of c_{33} is independent of n to within the experimental uncertainties. The uncertainty in c_{33} involves the uncertainty in the measurements of the echo time, density, and thickness. We estimate that the uncertainty in each of these parameters is 1.5%, leading to an overall uncertainty in c_{33} of $\approx 5\%$. The measured value of $c_{33} \approx 39$ GPa is in the middle of the range of c_{33} for disordered MoSe₂, $32 < c_{33} < 44$ GPa [9]. For comparison, c_{33} of disordered WSe₂ is $c_{33} \approx 25$ GPa [1].

The uncertainty in c_{44} involves contributions from the measurement of the SAW frequency and all of the parameters in the elasticity model [23]. The most important sources of uncertainties in the model are c_{11} , c_{33} , density, and thickness of the [SnSe]_{*n*}[MoSe₂]_{*n*} layer; and the density and thickness of the Al layer. We estimate that the combined uncertainties propagating from these parameters is 30% in the determination of c_{44} . The uncertainty of 1% in the measurement of SAW frequency, however, is more important than the uncertainties in the model parameters. We therefore set the error bars on the data points in Fig. 5(b) using a $\pm 1\%$ uncertainty in the frequency. The large uncertainty in c_{44} in comparison with our earlier publications using the same technique is because c_{44} of [SnSe]_{*n*}[MoSe₂]_{*n*} is small and v_{SAW} then becomes more sensitive to c_{33} than to c_{44} . Also, the overall sensitivity of the SAW frequency to the elastic constants of the layer is small because

TABLE III. Calculated and measured elastic constants of [SnSe]₁[MoSe₂]₁. The lattice constant c is measured by XRD; the elastic constant c_{33} is measured by picosecond acoustics; c_{44} is measured by SAW velocity.

	c (Å)	c_{11} (GPa)	c_{12} (GPa)	c_{13} (GPa)	c_{33} (GPa)	c_{44} (GPa)
DFT calculation	12.46	109	28	4.5	48	4.1
Experiment	12.43				39 ± 2	1.0 ± 0.4

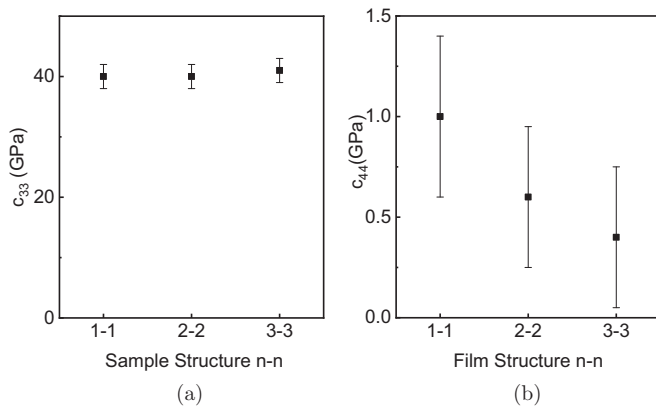


FIG. 5. (a) c_{33} of $[\text{SnSe}]_n[\text{MoSe}_2]_n$ for $n = 1, 2, 3$ measured by picosecond acoustics. (b) c_{44} of $[\text{SnSe}]_n[\text{MoSe}_2]_n$ for $n = 1, 2, 3$ measured by the frequency of SAWs with a wavelength of 700 nm and frequency of ≈ 4 GHz.

of the small thickness (60 nm) of the $[\text{SnSe}]_n[\text{MoSe}_2]_n$ layer compared to the acoustic wavelength (700 nm).

While the experimental uncertainties are comparable in magnitude to any trends in the data, the data plotted in Fig. 5(b) suggest that c_{44} of $[\text{SnSe}]_n[\text{MoSe}_2]_n$ decreases with increasing n . At $n = 1$, there are no turbostratic $\text{MoSe}_2/\text{MoSe}_2$ interfaces and the sample contains only incommensurate $\text{SnSe}/\text{MoSe}_2$ interfaces. As n increases, turbostratic disorder is introduced in MoSe_2 blocks. We previously reported our measurements of c_{33} and c_{44} of turbostratic MoSe_2 synthesized by the MER method: $c_{33} = 33$, $c_{44} = 3 \pm 1$ GPa [9]. Since c_{44} of turbostratic MoSe_2 is larger than c_{44} of $[\text{SnSe}]_n[\text{MoSe}_2]_n$, we cannot attribute a decrease

in c_{44} to a small shear modulus in thicker MoSe_2 blocks; furthermore, because the linear density of $\text{SnSe}/\text{MoSe}_2$ interfaces decreases with increasing n , we cannot directly attribute a decrease in c_{44} to small, independent of n , stiffness of $\text{SnSe}/\text{MoSe}_2$ interfaces. Our data suggest that the stiffness of the $\text{SnSe}/\text{MoSe}_2$ incommensurate interfaces decreases with increasing n , perhaps because it is easier for an $n = 1$ SnSe layer to arrange itself so that the Sn atoms are nested between Se atoms in the MoSe_2 layer. When n is larger, the SnSe layers are better crystallized and the nesting effect is less pronounced.

In conclusion, turbostratic disorder combined with incommensurate interfaces can significantly decrease the shear elastic constants c_{44} to ultralow values of ~ 1 GPa. Our experimental results help explain the exceptionally low thermal conductivity of disordered layered materials.

ACKNOWLEDGMENTS

D.Y.L. and D.G.C. acknowledge support from National Science Foundation Grant No. EFRI-1433467. A.S. acknowledges support from the National Science Foundation under Grant No. DMR-1555153. G.M. and D.C.J. acknowledge support from the National Science Foundation under Grant No. DMR-1710214. Pump probe measurements were carried out in the Laser and Spectroscopy Facility of the Materials Research Laboratory, University of Illinois. This work made use of the Illinois Campus Cluster, a computing resource that is operated by the Illinois Campus Cluster Program (ICCP) in conjunction with the National Center for Supercomputing Applications (NCSA) and which is supported by funds from the University of Illinois at Urbana-Champaign.

- [1] C. Chiritescu, D. G. Cahill, N. Nguyen, D. C. Johnson, A. Bodapati, P. Koblinski, and P. Zschack, *Science* **315**, 351 (2007).
- [2] N. S. Gunning, J. Feser, M. Beekman, D. G. Cahill, and D. C. Johnson, *J. Am. Chem. Soc.* **137**, 8803 (2015).
- [3] Z. Wei, Y. Chen, and C. Dames, *Appl. Phys. Lett.* **102**, 011901 (2013).
- [4] Z. Chen, Z. Wei, Y. Chen, and C. Dames, *Phys. Rev. B* **87**, 125426 (2013).
- [5] Z. Chen and C. Dames, *Appl. Phys. Lett.* **107**, 193104 (2015).
- [6] A. J. Minnich, *Phys. Rev. B* **91**, 085206 (2015).
- [7] H. Li, W. Zheng, and Y. K. Koh, *Phys. Rev. Mater.* **2**, 123802 (2018).
- [8] Z. Wei, F. Yang, K. Bi, J. Yang, and Y. Chen, *J. Phys. Chem. C* **122**, 1447 (2018).
- [9] E. C. Hadland, H. Jang, N. Wolff, R. Fischer, A. C. Lygo, G. Mitchson, D. Li, L. Kienle, D. G. Cahill, and D. C. Johnson, *Nanotechnology* (2019), doi: 10.1088/1361-6528/aafae2.
- [10] G. Savini, Y. J. Dappe, S. Oberg, J.-C. Charlier, M. I. Katsnelson, and A. Fasolino, *Carbon* **49**, 62 (2011).
- [11] R. Nicklow, N. Wakabayashi, and H. G. Smith, *Phys. Rev. B* **5**, 4951 (1972).
- [12] M. Grimsditch, *J. Phys. C: Solid State Phys.* **16**, L143 (1983).
- [13] C. Thomsen, H. T. Grahn, H. J. Maris, and J. Tauc, *Phys. Rev. B* **34**, 4129 (1986).
- [14] T. Pezeril, *Opt. Laser Technol.* **83**, 177 (2016).
- [15] J. A. Rogers, A. A. Maznev, M. J. Banet, and K. A. Nelson, *Annu. Rev. Mater. Sci.* **30**, 117 (2000).
- [16] D. Li, P. Zhao, J.-C. Zhao, and D. G. Cahill, *J. Appl. Phys.* **114**, 143102 (2013).
- [17] R. D. Westover, J. Ditto, M. Falmbigl, Z. L. Hay, and D. C. Johnson, *Chem. Mat.* **27**, 6411 (2015).
- [18] M. Beekman, G. Cogburn, C. Heideman, S. Rouvimov, P. Zschack, W. Neumann, and D. Johnson, *J. Electron. Mater.* **41**, 1476 (2012).
- [19] T. M. Phung, J. M. Jensen, D. C. Johnson, J. J. Donovan, and B. G. McBurnett, *X-Ray Spectrom.* **37**, 608 (2008).
- [20] L. Akselrud and Y. Grin, *J. Appl. Cryst.* **47**, 803 (2014).
- [21] K. Kang, Y. K. Koh, C. Chiritescu, X. Zheng, and D. G. Cahill, *Rev. Sci. Instrum.* **79**, 114901 (2008).
- [22] J. Liu, X. Wang, D. Li, N. E. Coates, R. A. Segalman, and D. G. Cahill, *Macromolecules* **48**, 585 (2015).
- [23] D. Li and D. G. Cahill, *Phys. Rev. B* **94**, 104306 (2016).
- [24] X. Du and J.-C. Zhao, *npj Comput. Mater.* **3**, 17 (2017).
- [25] J. P. Perdew, K. Burke, and M. Ernzerhof, *Phys. Rev. Lett.* **77**, 3865 (1996).

- [26] A. Tkatchenko and M. Scheffler, *Phys. Rev. Lett.* **102**, 073005 (2009).
- [27] G. Kresse and D. Joubert, *Phys. Rev. B* **59**, 1758 (1999).
- [28] G. Kresse and J. Furthmüller, *Phys. Rev. B* **54**, 11169 (1996).
- [29] G. Steinle-Neumann, L. Stixrude, and R. E. Cohen, *Phys. Rev. B* **60**, 791 (1999).
- [30] F. Birch, *Phys. Rev.* **71**, 809 (1947).
- [31] T. Chattopadhyay, J. Pannetier, and H. Von Schnering, *J. Phys. Chem. Solids* **47**, 879 (1986).
- [32] N. S. Gunning, J. Feser, M. Falmbigl, M. Beekman, D. G. Cahill, and D. C. Johnson, *Semicond. Sci. Technol.* **29**, 124007 (2014).
- [33] B. Evans and R. Hazelwood, *Phys. Status Solidi A* **4**, 181 (1971).
- [34] M. Ludemann, O. D. Gordan, D. R. Zahn, M. Beekman, R. Atkins, and D. C. Johnson, *Langmuir* **30**, 8209 (2014).
- [35] M. Falmbigl, M. B. Alemayehu, D. R. Merrill, M. Beekman, and D. C. Johnson, *Cryst. Res. Technol.* **50**, 464 (2015).
- [36] N. Wainfan and L. G. Parratt, *J. Appl. Phys.* **31**, 1331 (1960).
- [37] R. Atkins, D. B. Moore, and D. C. Johnson, *Chem. Mater.* **25**, 1744 (2013).
- [38] M. B. Alemayehu, M. Falmbigl, K. Ta, and D. C. Johnson, *Chem. Mater.* **27**, 2158 (2015).
- [39] See Supplemental Material at <http://link.aps.org/supplemental/10.1103/PhysRevMaterials.3.043607> for optical micrographs and atomic-force-microscope line scans of the MoS₂ flake.
- [40] E. I. Volkova, I. A. Jones, R. Brooks, Y. Zhu, and E. Bichoutskaia, *Phys. Rev. B* **86**, 104111 (2012).
- [41] J. L. Feldman, *J. Phys. Chem. Solids* **37**, 1141 (1976).